Diagnosing the seasonal land-atmosphere correspondence over Northern Australia: Dependence on soil moisture state and correspondence strength definition

Mark Decker[1] Andy Pitman[1] and Jason Evans[1]

[1] Climate Change Research Centre and ARC Centre of Excellence for Climate System Science, University of New South Wales

Correspondense to: Mark Decker (m.decker@unsw.edu.au)

Abstract

The strength of the correspondence between the land and the atmosphere during the onset (September) through to the peak (February) of the wet season over Northern Australia is statistically diagnosed using ensembles of offline land surface model simulations that produce a range of different background soil moisture states. We derive correspondence between the soil moisture and the planetary boundary layer via a statistical measure of association. The simulated evaporative fraction and the boundary layer are shown to be strongly associated during both SON and DJF despite the differing background soil moisture states between the two seasons and among the ensemble members. The sign and magnitude of the boundary layer-surface layer soil moisture association during the onset of the wet season (SON) differs from the correspondence between the evaporative fraction and boundary layer from the same season, and the correlation between the surface soil moisture and boundary layer coupling during DJF. The patterns and magnitude of the surface flux-boundary layer correspondence are not captured when the relationship is diagnosed using the surface layer soil moisture alone. The conflicting results arise because the surface layer soil moisture lacks strong association with the atmosphere during the monsoon onset because the evapotranspiration is dominated by transpiration. Our results indicate that accurately diagnosing correspondence and therefore coupling strength in seasonally dry regions, such as Northern Australia, requires root zone soil moisture to be included.

1 Introduction

The land surface influences the atmosphere at multiple spatial and temporal scales (Pitman 2003; Pielke et al., 2011; Williams and Maxwell, 2011). Land-atmosphere coupling strength is the degree to which land surface anomalies (e.g. soil moisture, vegetation characteristics, temperature, snow cover) lead to changes in atmospheric states and fluxes (e.g. rainfall, cloud cover, moisture convergence) as well as how anomalies in the atmosphere affect the land surface. The influence of land surface anomalies on atmospheric anomalies (and vice versa) proceeds through a chain of non-linear processes. The strength of these processes varies spatially and temporally and depend, in part, on the background state of the system (Betts 2004; Koster and Suarez, 2003; Taylor and Ellis 2006). The chain of mechanisms between soil moisture (SM) and precipitation (P) anomalies can be summarized following Santanello et al. (2011) as

$$\Delta SM \Rightarrow \Delta EF_{SM} \Rightarrow \Delta PBL \Rightarrow \Delta EF_{ATM} \Rightarrow \Delta CLD \Rightarrow \Delta P \qquad (1)$$

where the changes in soil moisture (ΔSM) lead to changes in evaporative fraction (ΔEF_{SM}), which alters the properties of the planetary boundary layer (ΔPBL) including the state (temperature, humidity) and the entrainment rate. These three near surface coupling mechanisms ($\Delta SM, \Delta EF_{SM},$ and ΔPBL) precede changes away from the land surface that further change evaporative fraction (ΔEF_{ATM}), leading to changes in cloud development and growth (ΔCLD), and ultimately forcing changes in precipitation (ΔP). The chain cycles with ΔP driving ΔSM to varying degrees depending on the region and season (Zhang et al. 2008). Equation (1) is a conceptualization of complex and nonlinear processes, such that the sign of the ΔCLD response to a ΔSM forcing can vary (Westra et al. 2012; Gentine et al. 2013). Equation (1) is a simplification of the short (less than a day) timescale coupling mechanisms and neglects large scale circulation and moisture feedbacks (Lee et al. 2012; Lintner and Neelin 2009; Lintner et al. 2013). Additional feedbacks that operate on short timescales not shown in (1), such as ΔEF_{SM} or ΔEF_{ATM} leading to ΔSM, may also be important (Seneviratne et al. 2010; Meng et al. 2014a,b). Despite simplifications, Equation (1) highlights the primary control SM exerts on EF as compared to secondary factors such as entrainment (Gentine et al. 2011). In a convective regime ΔSM initiates a series of events that first alter the atmosphere (ΔPBL) prior to changing P. The series of events from ΔSM-ΔPBL comprises the terrestrial portion of the coupling mechanisms and is the focus of this study, with coupling examined here limited to these processes. The ΔSM through ΔPBL sequence is a necessary, but not sufficient, set of processes that determine how P responds to changes in SM.

The sensitivity of atmospheric processes to ΔSM has been quantified with observations (Koster et al. 2003; Taylor and Ellis 2006) and multiple model experiments (Dirmeyer et al. 2006; Guo et al. 2006; Hirsch et al. 2013; Koster et al. 2000; Koster et al. 2006; Koster et al. 2011; Lee et al. 2012). Ferguson et al. (2012) combined multiple sources of reanalysis data with LCL and SM observations to examine the relationship between early morning surface layer SM (SM_l), and both the lifting condensation level (LCL) and the EF in the afternoon during the convective season. The relationship was quantified using the Kendall tau coefficient ($K\tau$), a non-parametric rank correlation coefficient that measures the association between two time series. Ferguson et al. (2012) found strong coupling ($K\tau$) between SM_l-EF, EF-LCL, and SM_l -LCL over many regions including monsoon regions such as Northern Australia. These three coupling mechanisms span the first three components in Equation (1) (ΔSM, ΔEF_{SM} and ΔPBL). While these represent only part of the processes involved in land-atmosphere coupling, they comprise a fundamental pathway by which SM anomalies drive an atmospheric response.

Several regional analyses have investigated the importance of land-atmosphere coupling in Northern Australia (Evans et al. 2011). Koster et al. (2000) showed land-atmosphere coupling increased the variance of P in both Northern and Eastern Australia. In agreement, Ferguson et al. (2012) found high correlations in SM_l-EF, EF-LCL, and SM_l-LCL during the convective (monsoon) season over the Northern savannas. These studies were limited in scope and did not explicitly explore how the coupling behaves during periods with different background climate states.

To examine land-atmosphere coupling strength we explore the correspondence between model derived soil moisture and water flux estimates with the observation based estimates of the boundary layer state. Significant association between soil moisture or surface fluxes and the atmosphere provides a necessary but not sufficient condition to demonstrate significant land-atmosphere coupling. The lack of land-atmosphere feedbacks in offline simulations means we cannot assess cause and effect, but by examining the statistical correspondence we can determine if the system states coevolve in a manner consistent with strong coupling. We focus on Northern Australia to examine whether the correspondence between soil moisture and the boundary layer can be diagnosed from SM_l in regions with a pronounced dry season, given the influence of groundwater on transpiration and deep SM variability (Decker et al. 2013). Northern Australia has a pronounced May to September dry season and a monsoon-driven wet season from November through February (Figure 1). The monsoonal climate allows us to examine the SM_l-LCL association as defined in Ferguson et al. (2012) in sharply contrasting seasons (Figure 1) that exhibit contrasting background soil moisture states. By examining the differences between correspondence during the onset (defined here as SON to coincide with the initial increase in rainfall) of the wet season when soil moisture will be low, and then through to the peak (defined as DJF to coincide with the precipitation maximum) of the wet season, we aim to determine the reliability of diagnosing the terrestrial and near surface stages of land-atmosphere correspondence using $K\tau$ derived from SM_l and LCL during periods where total ET fluxes are dominated by either soil evaporation or transpiration. The statistical association is defined here such that the land surface processes in Equation (1) (ΔSM, ΔEF_{SM} and ΔPBL) are examined, while the sequence of events in the atmosphere (ΔCLD and ΔP) are neglected. This terrestrial derived statistical association captures how ΔSM relates to state changes in the mixed layer (ΔPBL). Strong association as defined here is a necessary but not sufficient prerequisite for strong ΔSM-ΔP coupling. An ensemble of offline simulations using two model configurations, one of which neglects groundwater and therefore contains greatly reduced deep soil moisture, are driven using four forcing datasets. The simulations provide estimates of SM_l in addition to SM over the root zone (SM_{rz}), total ET and the ET components. Afternoon (2 pm local time) LCL is derived using the near surface atmospheric variables from the forcing datasets, and the sensitivity of the ensemble median $K\tau$ is examined for the onset and peak of the monsoon season.

This manuscript is organized as follows. The model simulations, the SM_l and ET observations used for model evaluation, and the near surface atmospheric datasets are summarized in Section 2.

Section 3 outlines the statistical measure of association used for coupling strength, the derivation of LCL from the atmospheric data, and the model experiments used to estimate the evaporative fraction and soil moisture. The Results section consists of the SM_l-LCL and EF-LCL based association strength, the impact of defining association strength with SM_{rrz} (the root zone SM) are presented in Section 4. The results are explained in terms of the governing physical processes and previous research in Section 5.

2 Model Simulations and Data

2.1 Near Surface Atmospheric and Forcing Data

The lifting condensation level (LCL see Section 3.2) over the entire study region is computed from combinations of near surface atmospheric data using two reanalysis products. The LCL is also calculated at the two flux sites using the tower observations. The model simulations (see Section 2.2) are driven using a combination of atmospheric states and fluxes from reanalysis products, a gauge based daily precipitation dataset, and a 3 hourly satellite-based precipitation product. We follow Decker et al. (2014) and utilize four forcing datasets to drive model simulations.

The two gridded sources of temperature, humidity, wind speed, pressure, and radiative fluxes are the Global Land Data Assimilation System (GLDAS, http://disc.sci.gsfc.nasa.gov/hydrology/data-holdings, Rodell at al., 2004) and the Modern-Era Retrospective Analysis for Research and Applications (MERRA) product (Bosilovich et al., 2008). These two datasets are utilized due to the high spatial resolution of GLDAS (0.25°) and high temporal resolution of MERRA (hourly). Two forcing datasets are comprised of the uncorrected GLDAS and MERRA data interpolated to a common $0.25^{\circ} \times 0.25^{\circ}$ grid. In addition two precipitation corrected datasets developed in Decker et al. (2014) are used. The uncorrected atmospheric states and radiative fluxes from MERRA are combined with P corrected via two algorithms. First, MERRA is corrected using the Australian Water Availability Project (AWAP) daily gridded precipitation data (Jones et al. 2009) to remove the monthly biases (labelled MERRA.B). Second, the MERRA precipitation is replaced with precipitation derived from disaggregating the daily AWAP data with the 3 hourly Tropical Rainfall Measuring Mission (TRMM) 3B42 (Huffman et al. 2007) data (labelled MERRA.BT). These two corrected datasets have identical monthly mean precipitation but different distributions of sub-monthly precipitation.

2.2 Simulated estimates of Soil Moisture and Evaporative Fraction

We use the community land model version 4 (CLM4, Oleson et al. 2010) to simulate the states and fluxes of water and energy using configurations documented in Decker et al. (2013; 2014). The land surface model simulations and reanalysis products allow for the terrestrial leg (ΔSM-ΔPBL in Equation (1)) to be explored explicitly. A detailed description of the groundwater configurations and modifications are given in Decker et al. (2014).

The suite of simulations is utilized to address forcing data and model configuration uncertainties in addition to exploring a large soil moisture state space. Two different configurations of CLM4 are used. The first consists of the default CLM4 (referred to as CTRL). The second (referred to as DRY) uses a modified CLM4 that replaces the two-way soil moisture coupling between the soil column and the aquifer with a free drainage bottom boundary condition. The modifications significantly reduce the soil moisture at depths below several centimeters and the ET flux during periods of low rainfall while not imparting large differences on the changes in total column water (Decker et al. 2014). The two model configurations thus enable the coupling between the atmosphere and the land surface to be examined under two differing background soil moisture states.

The CLM4 evapotranspiration is computed as the sum of the soil evaporation, the canopy evaporation and the transpiration. Transpiration is determined from the rate of photosynthesis and is, in part, a function of SM. The dependence on SM is determined by the soil water potential in each soil layer, the root distribution (prescribed by plant functional type, PFT), and the PFT dependence on water stress. The spatial distribution and phenology of PFTs are specified and identical across all simulations. The C3 grass PFT sets approximately 99% of the roots within 1m of the surface, while approximately 90% of the roots are within this depth for the broadleaf evergreen forest PFT.

The experiment design follows the simulations outlined in Decker et al. (2014) that have been shown to be in good agreement with observations over parts of Australia. One control (CTRL) simulation and one dry simulation are equilibrated for the period 1948-1979 using the corrected NCEP/NCAR data (Qian et al. 2006) after interpolating to the same 0.25° x 0.25° grid as the other forcing datasets. The CTRL and DRY simulations ending in 1979 provide initial conditions for the four CTRL and four DRY simulations from 1979-2007. The model evaluation period spans the five years coincident with the SM and ET data from 2003-2007. The associations are computed using the period 1990-2008. Both the CTRL and the DRY simulations are forced with the four forcing datasets (see Section 2.1): GLDAS, MERRA, MERRA.B, and MERRA.BT, generating a total of eight model simulations. The SM (from all model layers), and turbulent energy fluxes are output at three hourly intervals (coincident with the temporal resolution of the GLDAS forcing), while the remaining CLM4 output is saved as monthly means.

2.3 Validation Data: Soil Moisture and Evapotranspiration

The spatial-temporal behavior of the simulated surface soil moisture (SM_1) and evapotranspiration (ET) are validated against gridded observationally based estimates. SM_1 is evaluated against the daily Advanced Microwave Scanning Radiometer-Earth Observing System (AMSR-E) L3 surface SM product. The data are derived from passive microwave measurements and available for the period 2002 to 2011 (Njoku et al. 2003). AMSR-E based SM compares favorably with in-situ measurements over Australia (Draper et al. 2009) and exhibits spatiotemporal variability consistent with land model simulations (Liu et al. 2009). To simplify the comparison with the simulated SM, the first model layer (~0.7cm deep) SM is assumed comparable to SM from AMSR-E despite the uncertain effective measurement depth (approximately 1 cm) that varies with SM.

The simulated evapotranspiration is evaluated against three ET products. Multiple ET datasets based on different methodologies are included due to the uncertainty associated with deriving gridded moisture flux data (Jimenez et al. 2011). The Global Land Evaporation Amsterdam Methodology (GLEAM) (Miralles et al. 2010), the model-tree ensemble based dataset from MPI-Jena (J2010 hereafter) (Jung et al. 2010), and the Moderate Resolution Imaging Spectrometer (MODIS) MOD16 dataset (Mu et al. 2007; 2011) are used to estimate the observed mean seasonal ET fluxes. The observed ET is estimated using the arithmetic mean of the three datasets after the GLEAM and MOD16 data are aggregated to the coarse resolution (0.5° x 0.5°) of the J2010 data. The simulations are subsequently compared to the mean observed ET separately for the wet (December-February) and the end of the dry (September-November) seasons.

In addition to the gridded SM and ET datasets the model is evaluated against observations from two flux tower sites included in the OZ Flux network (ozflux.org.au). The Adelaide River site (Beringer, 2013a) spans November 2007 through May 2009 and is located at 13.08°S 131.12°E. The Howard Springs site (Beringer, 2013b) spans 2001 to present and is located at 12.48°S 131.15°E. Both sites provide air temperature, water vapor, surface pressure, radiation, turbulent fluxes (including ET), and soil moisture measurements at 30 minute intervals. The level 3 (L3) quality controlled data were utilized in this study. Adelaide River provides SM data at 5cm depth while Howard Springs provides SM at a depth from 10cm. The simulations are validated against the observed ET and SM at these two locations.

3 Methods

3.1 Kendall τ

We evaluate the land-atmosphere coupling strength using Kendall tau (Kτ), a non-parametric, rank correlation statistic (Press et al. 1992). Following Ferguson et al. (2012), Kτ is used to indicate the correspondence between two states important to land-atmosphere coupling. Kτ does not assume linearity between the variables being compared and tests for statistical significance. Kτ ranges from -1 to 1 (positive values indicate the temporal variations are synchronized), with statistical significance depending on the sample size (approximately 0.12 for the simulation based results in this study). Kτ is defined as

$$K_\tau = \frac{N_o - N_d}{0.5\mathrm{n}(n-1)} \qquad (2)$$

where N_o is the number of ordinate pairs, N_d is the number of disordinate pairs, and n is the number of observations. Ordinate pairs are pairs of numbers for which the change between them have the same sign, i.e. both are either positive or negative. The data are necessarily detrended separately over each season prior to deriving Kτ to prevent the strong seasonal cycle (Figures 2 and 3) from controlling the statistical relationship. The spatially distributed Kτ is calculated between the seasonally detrended three hourly modeled SM_l during the morning and the estimated three hourly LCL from the afternoon at each grid cell for each month during both the wet and dry seasons. Kτ is additionally derived with detrended data at two flux tower sites using measurements of SM and LCL estimated from the tower data. The morning SM_l is utilized because SM will be highest in the morning prior to decreasing during the day due to ET. The local time of SM and LCL varies because the simulations and forcing data utilize GMT. The distributed $K\tau$ is found separately for each of the eight simulated (See Section 2.2) estimates of SM_l and the four estimates of LCL (Section 3.2), generating a total of 32 estimates of $K\tau$ for each month in both the wet and dry seasons. The median $K\tau$ is found separately for the wet and dry seasons for the two different model configurations (Section 3.3) to give the final estimation of the correspondence. The association is also diagnosed using $K\tau$ between the model simulated afternoon evaporative fraction and the afternoon LCL. A second definition of association is found by calculating $K\tau$ between the morning time root zone SM (SM_{rz}) and the afternoon LCL (SM_{rz}-LCL). SM_{rz} is defined as the vertically averaged SM from the surface to a depth of 1m.

The physical meaning of a negative SM-LCL $K\tau$ association is as follows. A high value of SM will cause a larger ET flux, moistening the lower atmosphere, causing a lower LCL. Thus we hypothesis that in regions where the land-atmosphere are coupled the SM-LCL $K\tau$ should be negative. If SM has no association with LCL than Kt is expected to be statistically insignificant. Similarly, if ET is negatively associated with LCL ($Kt < 0$), it means that high ET may be moistening the lower atmosphere again leading to a lower LCL.

3.2 Calculation of Lifting Condensation Level

The state of the convective atmosphere is evaluated using the lifting condensation level (LCL), defined as the height (in pressure) that a parcel reaches saturation when ascending adiabatically from the surface. While a lower LCL is favorable to convection, it is not a sufficient constraint to guarantee it. For convection to occur a parcel must reach the level of free convection (LFC), which may not occur even if a parcel reaches the LCL. The height (in pressure) of the LCL is derived using only near surface variables under the assumption that the boundary layer is well developed and therefore well mixed. Estimating the LCL from near surface variables provides heights comparable to direct observations (Ferguson and Wood 2009). Under these assumptions, the pressure at the LCL is given by

$$LCL = P_{srf} - P_{srf}\left(\frac{T_{air}}{T_{dew}}\right)^{\frac{-c_p}{R}} \quad (3)$$

where P_{srf} is the surface pressure (Pa), T_{air} is the near surface air temperature (K), T_{dew} is the near surface dew point temperature (K), R is the specific gas constant of dry air (J K^{-1} kg^{-1}), and c_p is the specific heat of dry air at constant pressure (J K^{-1} kg^{-1}). Four spatially explicit estimates of LCL are found by applying Equation (4) to several combinations of near surface forcing data, and two point wise estimated are derived from the flux tower data. While P_{srf} and T_{air} are directly provided by both reanalysis products and the tower measurements, T_{dew} is calculated using the available near surface atmospheric states. The four distributed estimates of LCL are calculated with Equation (4) by: 1) using GLDAS for pressure and both temperatures, 2) using MERRA for pressure and both temperatures, 3) using pressure from MERRA and temperatures from GLDAS, and 4) using pressure from GLDAS and temperatures from MERRA. The LCL is quality controlled by limiting LCL to be less than the surface pressure.

4. Results

4.1 Validation of Simulated Soil Moisture and Evapotranspiration

The two model configurations are separately validated against the observationally estimated soil moisture and evapotranspiration on monthly and seasonal timescales, respectively. Figure 2a shows the timeseries of the area averaged (10-15S to 120-150E) normalized ensemble mean first layer soil moisture from the CTRL and the DRY ensembles and the AMSR-E observed data. The simulation dynamics are evaluated using the normalized SM_1 due to the difficulties in direct comparison of simulated and observed soil moisture (Koster et al. 2009). The strong seasonal cycle of soil moisture owing to the monsoonal climate is evident in both the observationally based estimates and the simulations. CTRL and DRY are nearly identical aside from the dry season in 2005 where the soil moisture in CTRL decreases more than that from DRY. The observed moistening of the soil following the dry seasons in Figure 2a occurs within a month to that of the simulated moistening. The mean monthly soil moisture closely follows that of the observationally based estimates and exhibits dynamic behavior independent of the model configuration.

The bias of the ensemble mean time averaged surface layer soil moisture from the eight simulations against the AMSR-E product is shown in Figure 2b. Over large regions of Northern Australia, the simulated SM_l is within 0.025 mm^3 mm^{-3} of AMSR-E. The difference in mean SM_l between the two model configurations is similarly small (figure not shown). Figure 2 demonstrates that the temporal evolution (Figure 2a) and mean state (Figure 2b) of the simulated SM_l are similar to the AMSR-E estimates.

The seasonal mean ET is validated against the arithmetic mean of the three gridded ET products for both DJF (Figures 3a, 3c, and 3e) and SON (Figures 3b, 3d, and 3f). The observed DJF ET (Figure 3e) has a strong north-south gradient with a maxima centered around 13ºS-130ºE. The strong north-south gradient is also present in the ensemble mean ET (Figure 3a), however the simulations overestimate DJF ET over much of the domain. The observationally based estimates show an ET of less than 50 Wm^{-2} south of 18ºS while the simulations remain above 60Wm^{-2} in this region. The mean SON ET is markedly lower compared to DJF ET in both the gridded data (Figure 3f) and the simulations (Figure 3b). Similar to DJF, both the model and the ET product show a strong north-south gradient. The simulations under estimate the ET in the York Peninsula (East of 140ºE and North of 17ºS) during SON and overestimate the ET in this region during DJF. The overestimation of DJF ET compared to the gridded product is much more pronounced for the CTRL simulations (Figure 3a) than the DRY simulations (Figure 3c). The underestimation of the SON ET in the simulations is largely a result of including the DRY model configuration. The CTRL simulations exhibit a 10-20 Wm^{-2} increase in SON ET over the DRY model runs (Figure 3b and Figure 3d). Overall, the model exhibits spatial-temporal ET in close agreement with this gridded ET product.

Point measurements of SM and ET at two locations show reasonable agreement with the model simulations. The Howard Springs SM observations 10cm depth (Figure 4a) typically increases from 0.05 to 0.2 mm^{3}mm^{-3} from the dry to the wet season. The observations are drier during the wet season and have a smaller (by a factor of two) seasonal cycle than both the DRY and CTRL simulations. DRY is much drier (~ 0.08 mm^{3}mm^{-3}) than CTRL (~0.18 mm^{3}mm^{-3}) during the dry season and in better agreement with the measurements (~0.05 mm^{3}mm^{-3}). This contrasts with the agreement at the

Adelaide River site (Figure 4b) where the measurements and CTRL peak around 0.30 mm^3mm^{-3} during the 2008 wet season. DRY (0.02-0.07 mm^3mm^{-3}) is again much drier than CTRL (0.15 mm^3mm^{-3}) during the 2008 dry season but CTRL is in better agreement with the data (0.15 mm^3mm^{-3}). The AMSR-E estimate, CTRL, and DRY are similar in Figures 4a and 4b (the Y-axis scale is the same in both figures), while the SM observations at the two sites differ drastically. The disagreement in the mean as well as the amplitude of the seasonal variability is likely due to both the difference in scale between the measurements and simulations and poor representation of soil properties in the model. When the SM comparison is normalized using the first two moments as in Figure 2a (not shown) there is greater agreement between the measurements, AMSR-E, and the simulations.

The ET data at Howard Springs (Figure 4c) demonstrates that the CTRL simulation always produces too little ET during the dry season. While the gridded ET estimate in Figure 4c falls within 10 Wm^{-2} of the CTRL simulation during the dry season, the tower data are nearly 20 Wm^{-2} greater than both during the 2007 and 2008 dry seasons. The wet season peak in ET is well simulated by both CTRL and DRY at Howard Springs. The model performance is different at Adelaide river as both CTRL and DRY have a wet season peak ET of around 120 Wm^{-2} while the measurements peak closer to 150 Wm^{-2}. Figure 4d further demonstrates that DRY has too little dry season ET.

The results from Figures 2, 3 and 4 demonstrate that CLM4 simulates the monthly and seasonal first layer soil moisture and evapotranspiration reasonably. While the details of the model performance vary depending on which site, season, and ensemble member is used for validation, overall the spatial and temporal patterns of ET and SM are generally captured by the modeling system. The accuracy of the estimated land surface states and fluxes therefore enables the use of the simulated variables in the diagnoses of the land-atmosphere association strength during SON and DJF.

4.2 Background SM state

The sharp contrast in background SM state can be illustrated by taking a spatial-temporal average of SM as a function of depth for CTRL and DRY for DJF (Figure 5a) and SON (Figure 5b). The soil moisture away from the surface is markedly different between CTRL and DRY. During DJF, CTRL shows a slight increase in soil moisture with depth, reaching a peak of ~0.35 mm^3mm^{-3} at depths near 3 m. In contrast, DRY has a peak soil moisture of only ~0.24 mm^3mm^{-3} at the surface and decreases with depth to near zero at 3 m. Similar patterns of SM with depth are seen over SON, however SM_1 is considerably lower for both CTRL and DRY compared to DJF.

Despite the similar mean and temporal behavior of SM_1 shown in Figure 2, SM away from the surface differs substantially between the two model configurations (Figure 3). The mean DJF ET is similar between CTRL and DRY, with differences between the two only 10-20 Wm^{-2}, corresponding to roughly 10-20% of the mean value. The fractional contribution of transpiration to the total ET during DJF is roughly 10-30% for both DRY and CTRL (figure not shown) indicating that the evaporation is the dominant ET mechanism. The enhanced mean SM in CTRL causes the CTRL ET to be greater than the DRY ET during DJF, yet both compare reasonable well to the observationally based estimates (Figure 3). However the lack of SM at depths below several centimeters for DRY during SON causes the reduced ET as compared to CTRL during this period. The mean ET during SON is sensitive to the mean SM away from the surface, indicating that transpiration significantly contributes to the total ET during this period. The reduced root zone SM in DRY leads to an increase in water stress and reduced transpiration. This reduction during SON is large relative to the mean ET during the period (Figure 3).

4.3 Correspondence: EF-LCL and SM_1-LCL

The statistical association between the evaporative fraction and the LCL is shown in Figure 6, with the results from the two flux towers shown in enclosed squares around 13^{O}N and 131^{O}E. The insignificant associations are greyed out while the statistically significant results are shown in color. During DJF, CTRL (Figure 6a) and DRY (Figure 6c) exhibit strong surface flux-atmosphere correspondence, with the strongest association over the Cape York Peninsula (East of 140°E and North of 17°S) and the Southwestern part of the domain. Similarly, the EF-LCL coupling is significant during SON (Figures 6b and 6d) over much of the domain, although the magnitude is reduced relative to DJF. Both ensembles show strong associations independent of the season, however the differences between CTRL and DRY vary with season. The DJF EF-LCL correspondence near 15°S 132°E is statistically significant in DRY (Figure 6c) but not in CTRL (Figure 6a), contrasting the similar SON EF-LCL association in this region exhibited by both DRY (Figure 6d) and CTRL (Figure 6b). The flux towers (boxed squares in Figures 6a-6c) both show statistically significant association between

EF and the LCL during both seasons. The EF-LCL correspondence from the tower observations agree more closely with DRY in DJF as CTRL show statistically insignificant association in the region (13°S 131°E). The reduced deep layer soil moisture resulting from the removal of the groundwater module enhances the DJF correspondence in agreement with the tower data.

Figure 7 shows the median Kendall tau (Kτ) between SM_l and the LCL (see Section 3.3) for CTRL and DRY separately during DJF (Figures 7a and 7c) and SON (Figures 7b and 7d). Several important features are present in Figure 7. The SM_l-LCL association during DJF and SON is largely similar between the two model configurations. CTRL (Figure 7a) and DRY (Figure 7c) exhibit similar spatial patterns and magnitudes of Kτ. Some regions (17°S 126°E) exhibit increases in the magnitude of Kτ in CTRL relative to DRY in DJF (Figures 7a and 7c) although the differences are statistically insignificant over most of the domain. Regardless of these slight variations in Kτ, CTRL and DRY exhibit a strong association between SM_l and the boundary layer during the peak of the wet season over coincident parts of the domain. Both model configurations also show areas (15°S 131°E) with insignificant correspondence adjacent to the strongly associated regions. In contrast, CTRL and DRY both contain regions of significant positive Kτ demonstrating a negative correspondence during SON, in disagreement with the results from the Adelaide River tower site. The tower sites both show statistically significant negative SM-LCL association during DJF adjacent to a region (15°S 131°E) of insignificant correspondence both simulations. The similarity in SM_l-LCL correspondence between CTRL and DRY during both DJF and SON implies a similar temporal variability of SM_l as related to the LCL. From Figure 3, the mean ET fluxes are considerably different during SON. The similar temporal behavior relative to the LCL for both DRY and CTRL indicates that the SM_l variability is physically independent of the season mean ET fluxes.

Contrasting Figures 6 and 7 reveals that the surface fluxes (Figures 6b and 6d) are associated with the LCL despite the simulated surface layer soil moisture (Figures 7b and 7d) lacking similar correspondence. The regions of positive Kτ in Figure 7 contradict the strongly negative Kτ in Figure 6 during SON. The flux towers show negative association for both EF-LCL and SM-LCL during DJF and SON in Figures 6 and 7. The EF-LCL coupling during DJF is much stronger that the SM_l

coupling, and DRY exhibits regions of stronger EF-LCL correspondence than CTRL, however the differences are not statistically significant over much of the domain. A key difference between the flux tower and model simulation estimated $K\tau$ is the depth of the SM. The measurement depth at the tower sites are 5cm and 10cm for Adelaide River and Howard Springs respectively, while the model surface layer soil moisture is taken from a depth of 0.7 cm. The change in sign of SM_l-LCL $K\tau$ from SON (Figures 7b and 7d) to DJF (Figures 7a and 7c) demonstrates that applying Equation (4) to SM_l and the LCL doesn't always capture the coupling between the land and the atmosphere during periods where deep SM and transpiration dominate the ET flux.

In short, our results demonstrate that the simulated surface layer soil moisture cannot adequately capture the SM-LCL association during both DJF and SON. The significant contributions of transpiration to the total ET fluxes (especially during SON) are responsive to perturbations in SM_{rz} and not SM_l.

4.6 Proposed Association strength definition: SM_{rz}-LCL

The definition of land-atmosphere coupling using land surface moisture states and fluxes must encompass the relevant physical mechanisms. Previously, Ferguson et al. (2012) was limited to using SM_l in deriving $K\tau$ because the AMSR-E (or other microwave) SM measurements typically measure to depths less than a few centimeters beneath the soil surface. Computing $K\tau$ between SM_l and the LCL incorporates the surface layer soil moisture that is important for surface evaporation from the soil. Therefore the DJF coupling (or other periods where the ET is largely comprised of soil evaporation) should be adequately defined using SM_l. $K\tau$ computed from SM_l neglects SM_{rz} variations that drive transpiration during the initial increase in precipitation following the dry season and therefore may not fully encompass the extent of land-atmosphere associations. Acknowledging the importance of transpiration during the Northern Australian wet season, we further evaluate the land-atmosphere association by computing $K\tau$ between the vertically averaged SM_{rz} and the LCL. As opposed to remotely sensed SM from AMSR-E (or other satellite products), the use of simulated SM facilitates the estimation of SM_{rz}. Applying Equation (4) using SM_{rz} imposes a different set of problems, as the rooting depth is model dependent and generally only approximately known. There is substantial evidence that eucalypts have rooting depths exceeding 20 meters (Schenk and Jackson 2002), however neither CLM4 nor the direct observations in this study extend that deep. Due to these limitations, SM_{rz} is computed as the weighted mean of the SM observations at 10, 40, and 100cm for the Howard Springs site. We assume that the SM_{rz} consists of the soil layers between the surface and a depth of 1m, as greater than 90% of the prescribed roots in CLM4 are within 1m of the surface (Oleson et al. 2010). This assumed rooting depth is consistent with the model formulation but not realistic given the rooting depths of eucalypts.

Figure 8 shows the ensemble median coupling strength diagnosed between SM_{rz} and the LCL. Comparing Figures 7 and 8 it is clear that including the portion of SM that partially controls transpiration increases the magnitude of the DJF SM-LCL associations and eliminates the region near 14°S 131°E with statistically insignificant correspondence (Figures 7a and 7c) despite soil evaporation contributing significantly to the simulated ET. Large differences between the SON SM_{rz}-LCL and SM_1-LCL $K\tau$ are seen south of 15°S and east of 130°E. Despite large regions of statistically significant SON SM_{rz}-LCL $K\tau$ for CTRL (Figure 8b) and DRY (Figure 8d) regions of insignificant association are prevalent near 13°S 131°E. The flux tower derived SON SM_{rz}-LCL correspondence is insignificant in agreement with the DRY and CTRL results near 13°S 131°E. The similarity between the DRY and CTRL SM_{rz}-LCL $K\tau$ highlights the negligible groundwater impact (Figures 8b and 8d). Comparing Figures 8b and 8d with Figure 3b and 3d reveals that despite the impact of groundwater on the mean ET flux over SON, the mean state of the deep SM imparts little influence on the temporal dynamics of SM_{rz} in relation to the LCL. Neglecting the SM beneath the surface layer in the calculation of $K\tau$ results in a weak diagnosed SM-LCL association during SON because transpiration is partly governed by the water availability within the root zone. By defining the association using SM_{rz} it is clear that the land is strongly linked to the LCL during both DJF and SON. The DJF SM-LCL association in CTRL near flux tower sites is stronger when defined in this manner, although both sets of simulations still show SM_{rz} to be statistically associated to the LCL.

The SM_1-LCL, and SM_{rz}-LCL $K\tau$ shown in Figures 7, and 8 are the median from ensembles with 32 estimates. The ensembles explicitly use multiple constructions of LCL to sample the possible range atmospheric states given the near surface MERRA and GLDAS estimates, and may lead to uncertain estimates of $K\tau$. The inter-ensemble uncertainty of the $K\tau$ metric is examined to demonstrate the robustness of the results. The standard deviation of the coupling strength between SM_{rz} and the LCL and between SM_1 and the LCL among the ensemble members is generally less than 0.15 (Figures 8a-8d). The variation among the ensemble members is smaller than the median coupling strength shown in Figures 7 and 8. The low standard deviation relative to the median demonstrates that the association shown in Figures 7 and 8 is robust in that greater than 83% of the $K\tau$ estimates (assuming they are normally distributed) have a correspondence of the same sign reported in the figures. The coupling using SM_1 (Figure 8c) show larger ensemble uncertainty near the coast centered around 135E compared to the SM_{rz} coupling in DJF (Figure 8a) and over the Cape York Peninsula in SON (Figures 8b and 8a). Aside from the region near 15S and 130E during SON, the larger ensemble uncertainty is found when using SM_1 to define the coupling strength.

5 Discussion

The seasonal ET from CTRL, DRY, and the gridded ET products from DJF through SON provide insight into the mechanisms that limit the SON DRY ET. The ET from CTRL and DRY are similar (within +/- 10%) during the large DJF precipitation forcing. The dry season commences between MAM and JJA (Figure 1) resulting in increased vapor pressure deficit (VPD) between the vegetation and the atmosphere and increased photosynthetically active radiation (PAR). The changes in VPD and PAR promote increased transpiration from DJF through MAM, although the actual transpiration is also governed by SM_{rz}. Comparing Figure 3 and Figure 5 indicates that the DRY ET is relatively SM limited and unable to maintain ET similar in magnitude to CTRL and the observationally based estimates during SON. Within the model, the soil column-groundwater interactions parameterized in CTRL inhibit the large, ET limiting SM_{rz} reduction present in DRY. In reality the inability of DRY to maintain ET during SON may result from the shallow rooting depths assumed in CLM4. The depths are substantially shallower than the rooting depths of eucalypts. Realistic rooting depth profiles reaching nealy 20 meters in Australia (Schenk and Jackson 2002) and corresponding soil layer depths may negate the impact of the parameterized soil column-groundwater impacts current in CLM4.

The EF-LCL association (Figure 6) is similar for both model configurations despite the mean ET (Figure 3) and SM (Figure 5) differing considerably between CTRL and DRY. The similarity holds for both DJF and SON despite the differing background soil moisture states between the two periods. The results indicate that while the mean ET is a strong function of mean soil moisture, the SM-LCL coupling as diagnosed here is insensitive to the background state. The coincidence of the temporal variations in SM, EF, and LCL are demonstrated by the large values of Kτ. These seemingly counterintuitive results may be an artifact of using a rank correlation coefficient to determine the strength of the correspondence. Kτ only measures the temporal coincidence of the two time-series while neglecting the magnitude of these variations. Although Kτ is largely independent to the background soil moisture state, alternative definitions of association may not remain as invariant.

While association in Figure 6 is largely unaffected by the mean SM state, the mean ET flux is largely derived from deeper SM through transpiration during the onset of the wet season prior to DJF. Correspondence under these conditions is poorly defined using SM_l. The strong EF-LCL coupling during SON and DJF highlights the inadequacy of coupling diagnosed with SM_l. The physically improbable SM_l-LCL coupling varies from positive (Figure 5b) to negative (Figure 5a) as the wet season is established (Figure 1). Despite the domain mean precipitation increasing from roughly zero to several mm/day during SON, Kτ from SM_l-LCL exhibits both positive (i.e. 15°S 126°E) and negative (i.e. 15°S 134°E) coupling over this period. The transition from negligible (or positive) to strong land-atmosphere association during the wet season is an artifact resulting from the use of SM_l. More consistent correspondence in general agreement with the EF-LCL dynamics throughout the wet season exists between SM_{rz}-LCL because transpiration is incorporated into the coupling diagnostic. During SON, the dry surface layer SM is responsible for little ET, with variations in ET not associated with SM_l. The SM_{rz}-LCL Kτ eliminates the insignificant association around 17°S 128°E exhibited in the SM_l-LCL association. Despite regions of significant SM_{rz}-LCL association in DRY and CTRL, the Howard Springs data show insignificant SM_{rz}-LCL correspondence during SON. The lack of observed association is possibly related to the inability to sample SM at depths that correspond to the physically relevant rooting depths. The necessity of using SM_{RZ} agrees with Lee et al. (2012) where transpiration was found to limit precipitation variability over tropical regions. The importance of transpiration among the various ET components is not limited to Northern Australia or monsoon regions (Coenders-Gerrits et al. 2014; Schlesinger and Jasechko 2014) highlighting the need to characterize land-atmosphere dynamics using SM well beneath the surface.

Statistically determining the association using only near surface variables from land surface model simulations of SM and atmospheric data as done in this study (i.e. Ferguson et al. 2013, Betts 2004) is limited due to only examining a part of the full land-atmosphere coupling processes. While the LCL is an important determinant in the formation of precipitation, moisture convergence, upper level inversions, convective available potential energy, wind shear, and many other factors play important roles in the formation of convection. The correspondence diagnosed in this study with Equation (4) is by definition limited in scope to only part of the coupling continuum described in Equation (1). Therefore association defined using these methods provides a necessary but not sufficient condition for strong land-atmosphere interactions between soil moisture and precipitation.

Our results likely extend to monsoonal regions beyond Northern Australia. GLACE (Koster et al. 2006) revealed multiple areas of strong land-atmosphere coupling coincide with major monsoon systems. The strong coupling during the wet season (September-February) diagnosed using SM_{rz} and $K\tau$ in our results qualitatively agrees with the strong coupling in monsoon regions from GLACE. The dry season antecedent to the large precipitation fluxes induces low evaporation while allowing deeply rooted plants to transpire despite the prolonged dry period. These conditions over Northern Australia (Figures 3 and 4) lead to transpiration dominating the ET flux during the onset of the wet season. Coupling diagnosed using $K\tau$ under these conditions must be defined using SM_{rz} rather than SM_1 to ensure the relevant pathways of the moisture fluxes are not neglected.

6 Conclusions

The land-atmosphere coupling strength is analyzed utilizing ensembles of land surface simulations and near surface atmospheric data. Using four forcing datasets, ensembles of CLM simulations over Northern Australia are performed, using configurations that either include or neglect soil column-groundwater interactions. The seasonal dynamics of the simulated SM_1 is insensitive to the mean soil moisture state and all simulations compare favorably with the AMSR-E soil moisture product. Further, the simulated ET from December to February is similar between the CTRL and DRY runs, with both configurations largely consistent with the DJF ET estimated from three gridded ET products.

The strength of the land-atmosphere association is diagnosed between both SM_l and EF from the simulations and the LCL as calculated from the near surface atmospheric state. During the peak wet season strong SM_l-LCL and EF-LCL associations are shown. The wet season onset (SON) shows strong EF-LCL association that contrasts the weak SM_l-LCL association demonstrating the SON coupling is not properly characterized with SM_l. The land-atmosphere interactions during periods with non-negligible transpiration necessitates the use of root zone soil moisture instead of the surface soil moisture to properly capture the physical processes. Properly defining the association with SM_{rz} differs considerably from the SM_l diagnosed association and shows strong associations throughout the wet season. The SM_{rz}-LCL association is consistent with that from EF-LCL. It should be noted that these associations are a necessary but not sufficient condition to diagnose full land-atmosphere coupling.

Our results also show that the diagnosed land-atmosphere coupling is insensitive to the mean vertical profile of soil moisture. It is however, sensitive to the depth of the soil column considered. The implication of our findings therefore indicates a need to include the root zone in order capture periods when the ET is dominated by transpiration. We recommend that future studies of land-atmosphere coupling should include groundwater and focus on root zone soil moisture rather than surface layer soil moisture.

Acknowledgments

We acknowledge support from the Australian Research Council Super Science scheme (FS100100054). AJP was also supported by the Australian Research Council Centre of Excellence for Climate System Science (CE110001028). JPE was supported by an Australian Research Council Future Fellowship (FT110100576). The GLDAS data used in this study were acquired as part of the NASA's Earth-Sun System Division and archived and distributed by the Goddard Earth Sciences

(GES) Data and Information Services Center (DISC) Distributed Active Archive Center (DAAC). We also thank Diego Miralles for providing the GLEAM ET product.

References

Betts, A. K. 2009: Land-Surface-Atmosphere Coupling in Observations and Models. *J. Adv. Model. Earth Syst.*, **1 (3)**, doi:10.3894/JAMES.2009.1.4.

Betts, A. K., J. H. Ball, A. C. M. Beljaars, M. J. Miller, and P. A. Viterbo. 1996: The Land Surface-atmosphere Interaction: A Review Based on Observational and Global Modeling Perspectives, *J. Geophys. Res-Atmos.*, **101 (D3)**, 7209–7225. doi:10.1029/95JD02135.

Betts, A. K., B. Helliker, and J. Berry, 2004: Coupling Between CO2, Water Vapor, Temperature, and Radon and Their Fluxes in an Idealized Equilibrium Boundary Layer over Land, *J. Geophys. Res.-Atmos.*, **109 (D18)**, doi:10.1029/2003JD004420.

Beringer, J., 2013a: Adelaide River OzFlux tower site OzFlux: Australian and New Zealand Flux Research and Monitoring hdl: 102.100.100/14228

Beringer, J., 2013b: Howard Springs OzFlux tower site. OzFlux: Australian and New Zealand Flux Research and Monitoring. hdl: 102.100.100/14234

Bosilovich, M. G., J. Chen, F. R. Robertson, and R. F. Adler, 2008: Evaluation of Global Precipitation in Reanalyses, *J. Appl. Meteor. Climatol.*, **47 (9)**, 2279–2299.

Coenders-Gerrits, A. M. J., van der Ent, R. J., Bogaard, T. A., Wang-Erlandsson, L., Hra- chowitz, M., and Savenije, H. H. G., 2014: Uncertainties in transpiration estimates, *Nature*, **506**, doi:10.1038/nature12925.

Decker, M., and X. Zeng. 2009: Impact of Modified Richards Equation on Global Soil Moisture Simulation in the Community Land Model (CLM3.5), *J. Adv. Model. Earth Syst.*, **1 (3)**, doi:10.3894/JAMES.2009.1.5.

Decker M., A. Pitman, J. P. Evans, 2013: Groundwater constraints on simulated transpiration variability over Southeastern Australian forests, *J. Hydrometeor.*, **14**, 543–559.

Decker M., A. Pitman, J. P. Evans, 2014: Applying scaled vegetation greenness metrics to constrain simulated transpiration anomalies: A study over Australia ,*J. Hydrometeor*, **15**, 1607–1623.

Dirmeyer, Paul A., Xiang Gao, Mei Zhao, Zhichang Guo, Taikan Oki, Naota Hanasaki, 2006: GSWP-2: Multimodel Analysis and Implications for Our Perception of the Land Surface, *Bull. Amer. Meteor. Soc.*, **87**, 1381–1397, doi: http://dx.doi.org/10.1175/BAMS-87-10-1381

Draper, C. S., J. P. Walker, P. J. Steinle, R. A.M. de Jeu, and T. R.H. Holmes, 2009: An Evaluation of AMSR-E Derived Soil Moisture over Australia, *Remote Sens. Environ.*, **113 (4)**, 703–710.

Eamus, D., and R. Froend. 2006: Groundwater-dependent Ecosystems: The Where, What and Why of GDEs, *Aust. J. Bot.*, **54 (2)**, 91–96.

Evans, J. P., A. J. Pitman, and F. T. Cruz, 2011: Coupled atmospheric and land surface dynamics over southeast Australia: A review, analysis and identification of future research priorities. *International Journal of Climatology*, **31**, 1758–1772, doi:10.1002/joc.2206.

Fan, Y., G. Miguez-Macho, C. P. Weaver, R. Walko, and A. Robock, 2007: Incorporating Water Table Dynamics in Climate Modeling: 1. Water Table Observations and Equilibrium Water Table Simulations, *J. Geophys. Res.-Atmos.*, **112 (D10)**, doi:10.1029/2006JD008111.

Ferguson, C. R., and E. F. Wood, 2009: Observing land–atmosphere interaction globally with satellite remote sensing, Proc. Earth Observation and Water Cycle Science Symp., Frascati, Italy, European Space Agency, P17.

Ferguson, C. R., E. F. Wood, and R. K. Vinukollu, 2012: A Global Intercomparison of Modeled and Observed Land-Atmosphere Coupling, *J. Hydrometeor.*, **13 (3)**, 749–784, doi:10.1175/JHM-D-11-0119.1.

Gedney, N., and P. M. Cox, 2003: The Sensitivity of Global Climate Model Simulations to the Representation of Soil Moisture Heterogeneity, *J. Hydrometeor.*, **4 (6)**, 1265–1275.

Gentine, P., D. Entekhabi, and J. Polcher, 2011: The Diurnal Behavior of Evaporative Fraction in the Soil–Vegetation–Atmospheric Boundary Layer Continuum, *J. Hydrometeor.*, **12**, 1530-1546.

Gentine, P., A. A. M. Holtslag, F. D'Andrea, and M. Ek, 2013: Surface and Atmospheric Controls on the Onset of Moist Convection over Land. *J. Hydrometeor*, **14**, 1443–1462.

Guo, Z., and Coauthors, 2006: GLACE: The Global Land–Atmosphere Coupling Experiment. Part II: Analysis. *J. Hydrometeor*, 7, 611–625, doi: http://dx.doi.org/10.1175/JHM511.1.

Hirsch, A., J. Kala, A. J. Pitman, C. Carouge, J. P. Evans, V. Haverd, and D. Mocko, 2013: Impact of Land Surface Initialisation Approach on Sub-seasonal Forecast Skill: A Regional Analysis in the Southern Hemisphere, *J. Hydrometeor.*, under review.

Huffman, G. J., D. T. Bolvin, E. J. Nelkin, D. B. Wolff, R. F. Adler, G. Gu, Y. Hong, K. P. Bowman, and E. F. Stocker, 2007: The TRMM Multisatellite Precipitation Analysis (TMPA): Quasi-Global, Multiyear, Combined-Sensor Precipitation Estimates at Fine Scales, *J. Hydrometeor.*, **8 (1)**, 38–55. doi:10.1175/JHM560.1.

Jimenez, C., and Coauthors, 2011: Global Intercomparison of 12 Land Surface Heat Flux Estimates, *J. Geophys. Res.*, **116**, D02102, doi:10.1029/2010JD014545.

Jones, D. A., W. Wang, and R. Fawcett, 2009: High-quality spatial climate data-sets for Australia, *J. Aust. Meteor. Oceanograp.*, **58**, 233-248.

Jung, M., and Coauthors, 2010: Recent Decline in the Global Land Evapotranspiration Trend Due to Limited Moisture Supply, *Nature*, **467**, 951–954, doi:10.1038/nature09396.

Koster, R. D., M. J. Suarez, and M. Heiser. 2000: Variance and Predictability of Precipitation at Seasonal-to-Interannual Timescales, *J. Hydrometeor.*, **1 (1)**, 26–46.

Koster, R. D., and M. J. Suarez, 2003: Impact of Land Surface Initialization on Seasonal Precipitation and Temperature Prediction, *J. Hydrometeor.*, **4 (2)**, 408–423.

Koster, R. D., and Coauthors, 2006: GLACE: The Global Land–Atmosphere Coupling Experiment. Part I: Overview. *J. Hydrometeor*, **7**, 590–610.

Koster, R. D., Z. Guo, R. Yang, P. A. Dirmeyer, K. Mitchell, and M. J. Puma, 2009: On the Nature of Soil Moisture in Land Surface Models, *J. Clim.*, **22**, 4322-4335.

Koster, R. D., and Coauthors, 2011: The Second Phase of the Global Land-Atmosphere Coupling Experiment: Soil Moisture Contributions to Subseasonal Forecast Skill, *J. Hydrometeor.*,**12 (5)**, 805–822. doi:10.1175/2011JHM1365.1.

Lee, J.-E., and Coauthors, 2012: Reduction of tropical land region precipitation variability via transpiration, *Geophys. Res. Lett.*, **39**, L19704, doi:10.1029/2012GL053417.

Lintner, B. R. and J. D. Neelin, 2009: Soil Moisture Impacts on Convective Margins. *J. Hydrometeor*, **10**, 1026–1039.

Lintner, B. R., P. Gentine, K. L. Findell, F. D'Andrea, A. H. Sobel, and G. D. Salvucci, 2013: An Idealized Prototype for Large-Scale Land–Atmosphere Coupling. *J. Climate*, **26**, 2379–2389.

Lo, M.-H., and J. S. Famiglietti, 2010: Effect of water table dynamics on land surface hydrologic memory, *J. Geophys. Res.*, ***115**, D22118, doi:10.1029/2010JD014191*.

Meng X.H., Evans J.P., McCabe M.F. (2014a) The Impact of Observed Vegetation Changes on Land–

Atmosphere Feedbacks During Drought. *J Hydrometeor.*, ***15***, 759–776. doi: 10.1175/JHM-D-13-0130.1

Meng, X. H., Evans, J. P. and McCabe, M. F. (2014b): The influence of inter-annually varying albedo on regional climate and drought, Clim Dyn, 42(3-4), 787–803, doi:10.1007/s00382-013-1790-0.

Miralles, D. G., R. A. M. De Jeu, J. H. Gash, T. R. H. Holmes, and A. J. Dolman. 2011: Magnitude and Variability of Land Evaporation and Its Components at the Global Scale, *Hydrol. Earth Syst. Sc.*, **15 (3)**, 967–981, doi:10.5194/hess-15-967-2011.

Miralles, D. G., T. R. H. Holmes, R. A. M. De Jeu, J. H. Gash, A. G. C. A. Meesters, and A. J. Dolman, 2010: Global Land-surface Evaporation Estimated from Satellite-based Observations, *Hydrol. Earth Syst. Sc.*, **7 (5)**, 8479–8519. doi:10.5194/hessd-7-8479-2010.

Mu, Q., F. A. Heinsch, M. Zhao, and S. W. Running, 2007: Development of a global evapotranspiration algorithm based on MODIS and global meteorology data, *Remote Sens. Environ.*, **111**, 519-536, doi:10.1016/j.rse.2007.04.015.

Mu, Q., L. A. Jones, J. S. Kimball, K. C. McDonald and S. W. Running, 2009: Satellite assesment of land surface evapotranspiration for the pan-Arctic domain, *Water Resour. Res.*, **45**, doi:10.1029/2008WR007189.

Niu, G.-Y., Z.-L. Yang, R. E. Dickinson, L. E. Gulden, and H. Su, 2007: Development of a Simple Groundwater Model for Use in Climate Models and Evaluation with Gravity Recovery and Climate Experiment Data, *J. Geophys. Res.-Atmos.*, **112 (D7)**, doi:10.1029/2006JD007522.

Njoku, E.G., T.J. Jackson, V. Lakshmi, T.K. Chan, and S.V. Nghiem, 2003: Soil Moisture Retrieval from AMSR-E, *Geoscience and Remote Sensing, IEEE Transactions,* **41 (2)**, 215–229, doi:10.1109/TGRS.2002.808243.

Oleson, K., and Coauthors, 2010: Technical Description of Version 4.0 of the Community Land Model (CLM), Http://dx.doi.org/10.5065/D6FB50WZ, http://nldr.library.ucar.edu/repository/collections/TECH-NOTE-000-000-000-848.

Pielke, R. A., and Coauthors, 2011: Land Use/land Cover Changes and Climate: Modeling Analysis and Observational Evidence, *WIRES. Clim.*, **2 (6)**, 828–850. doi:10.1002/wcc.144.

Pitman, A. J. 2003: The Evolution of, and Revolution in, Land Surface Schemes Designed for Climate Models, *Int. J. Climatol.*, **23 (5)**, 479–510, doi:10.1002/joc.893.

Press, W. H., B. P. Flannery, S. A. Teukolsky, and W. T. Vetterling, 1992: Nonparametric or rank correlation, Numerical Recipes in C: The Art of Scientific Computing, L. Cowles and A. Harvey, Eds., 2nd ed. Cambridge University Press, 639–644.

Qian, T., A. Dai, K. E. Trenberth, and K. W. Oleson. 2006: Simulation of Global Land Surface Conditions from 1948 to 2004. Part I: Forcing Data and Evaluations, *J. Hydrometeor.*, **7 (5)**, 953–975, doi:10.1175/JHM540.1.

Rodell, M., and Coauthors, 2004: The Global Land Data Assimilation System, *Bull. Amer. Meteor. Soc.*, **85 (3)**, 381–394, doi:10.1175/BAMS-85-3-381.

Santanello, J. A., C. D. Peters-Lidard, and S. V. Kumar, 2011: Diagnosing the Sensitivity of Local Land-Atmosphere Coupling via the Soil Moisture-Boundary Layer Interaction, *J. Hydrometeor.*, **12 (5)**, 766–786, doi:10.1175/JHM-D-10-05014.1.

Schenk, H. J., and R. B. Jackson, 2002: The Global Biogeography of Roots, *Ecol. Monographs*, **73**, 311-328.

Schlesinger, W. H. and Jasechko, S., 2014: Transpiration in the global water cycle, *Agr. Forest Meteorol.*, **189–190**, 115–117, doi:10.1016/j.agrformet.2014.01.011.

Seneviratne, S. I., T. Corti, E. L. Davin, M. Hirschi, E. B. Jaeger, I. Lehner, B. Orlowsky, and A. J. Teuling, 2010: Investigating Soil Moisture-climate Interactions in a Changing Climate: A Review, *Earth-Science Reviews*, **99**, 125–161, doi:10.1016/j.earscirev.2010.02.004.

Small, E. E., and S. A. Kurc, 2003: Tight Coupling Between Soil Moisture and the Surface Radiation Budget in Semiarid Environments: Implications for Land-atmosphere Interactions, *Water Resour. Res.*, **39 (10)**, doi:10.1029/2002WR001297.

Taylor, C.r M., and R. J. Ellis, 2006: Satellite Detection of Soil Moisture Impacts on Convection at the Mesoscale, *Geophys. Res. Lett.*, **33 (3)**, doi:10.1029/2005GL025252.

Vergnes, J.-P., B. Decharme, R. Alkama, E. Martin, F. Habets, and H. Douville, 2012: A Simple Groundwater Scheme for Hydrological and Climate Applications: Description and Offline Evaluation over France, *J. Hydrometeor.*, **13 (4)**, 1149–1171, doi:10.1175/JHM-D-11-0149.1.

Westra, D., G. J. Steeneveld, and A. A. M. Holstag, 2012: Some Observational Evidence for Dry Soils Supporting Enhanced Relative Humidity at the Convective Boundary Layer Top, *J. Hydrometeor.*, **13**, 1347-1358.

Williams, J. L., and R. M. Maxwell, 2011: Propagating Subsurface Uncertainty to the Atmosphere Using Fully Coupled Stochastic Simulations, *J. Hydrometeor.*, **12 (4)**, 690–701, doi:10.1175/2011JHM1363.1.

Yu, Z., Da. Pollard, and L. Cheng, 2006: On Continental-scale Hydrologic Simulations with a Coupled Hydrologic Model, *J. Hydrology*, **331**, 110–124, doi:10.1016/j.jhydrol.2006.05.021.

Zeng, X., and M. Decker, 2009: Improving the Numerical Solution of Soil Moisture–Based Richards Equation for Land Models with a Deep or Shallow Water Table. *J. Hydrometeor*, **10**, 308-319.

Zhang, J., W.-C. Wang, and J. Wei, 2008: Assessing Land-atmosphere Coupling Using Soil Moisture from the Global Land Data Assimilation System and Observational Precipitation, *J. Geophys. Res.-Atmos.*, **113**, doi:10.1029/2008JD009807.

List of Figures

Figure 1. Observations of the domain (18°S-11°S and 120ºE-150ºE) averaged mean annual cycle of precipitation (P in mm day^{-1}).

Figure 2. (a) The mean normalized (using the first two moments) first layer soil moisture (SM_1) from the CTRL and DRY simulations and the AMSR-E observations. (b) The difference between the mean SM_1 (from all simulations over all months from 2004-2009) and the AMSR-E observations.

Figure 3. The mean ET (Wm^{-2}) from the wet season (DJF shown in the left hand column) and the transition between the dry and wet seasons (SON shown in the right hand column). The ensemble mean ET from (a) CTRL over DJF, (b) CTRL over SON, (c) DRY for DJF, (d) DRY from SON, (e) OBS (the mean of three gridded ET products) over DJF, and (f) OBS for SON.

Figure 4. The monthly soil moisture (SM in mm^{3}mm^{-3}) from the ensemble mean from CTRL and DRY, AMSR-E, and flux tower measurements (OBS_{tower}) from flux tower sites at (a) Howard Springs at 10cm depth and (b) Adelaide River at 5cm depth. The monthly evapotranspiration (ET Wm^{-2}) from CTRL, DRY, the mean of three ET products ($OBS_{gridded}$) and the measurements at the (c) Howard Springs and (d) Adelaide River flux tower sites.

Figure 5. Spatiotemporal mean soil moisture (mm3mm-3) SM as a function of depth (m) for (a) DJF and (b) SON.

Figure 6. The ensemble median Kendall-tau correlation metric (Kτ) between the afternoon time (local) evaporative fraction (EF) and the afternoon computed lifting condensation level (LCL) at from (a) CTRL over DJF, (b) CTRL from SON, (c) DRY over DJF, and (d) DRY from SON. The black-outlined squares in (a)-(d) denote the values from the flux tower sites. Only statistically significant (95% confidence level) results are shown in (a)-(d).

Figure 7. The ensemble median Kendall-tau correlation metric (Kτ) between the morning first layer soil moisture (SM_1) and the afternoon computed lifting condensation level (LCL) from (a) CTRL over

DJF, (b) CTRL from SON, (c) DRY over DJF, and (d) DRY from SON. The black-outlined squares in (a)-(d) denote the values from the flux tower sites. Only statistically significant (95% confidence level) results are shown in (a)-(d).

Figure 8. The ensemble median Kendall-tau correlation metric ($K\tau$) between the morning root zone soil moisture (SM_{rz}) and the afternoon computed lifting condensation level (LCL) from (a) CTRL over DJF, (b) CTRL from SON, (c) DRY over DJF, and (d) DRY from SON. The black-outlined squares in (a)-(d) denote the values from the Howard Springs flux tower site. Only statistically significant (95% confidence level) results are shown in (a)-(d).

Figure 9. The standard deviation of the Kendall-tau correlation metric ($K\tau$) among the ensemble members between the afternoon computed lifting condensation level (LCL) and either the morning root zone soil moisture (SM_{rz}) over (a) DJF, (b) SON, or the morning first layer soil moisture (SM_1) over (c) DJF, and (d) SON.

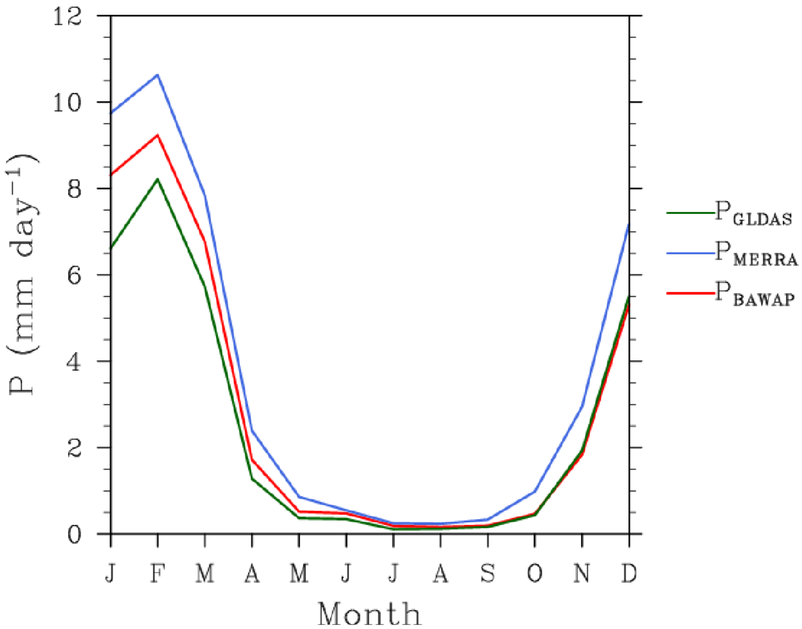

Figure 1. Observations of the domain (18ºS-11ºS and 120ºE-150ºE) averaged mean annual cycle of (a) precipitation (P in mm day^{-1}).

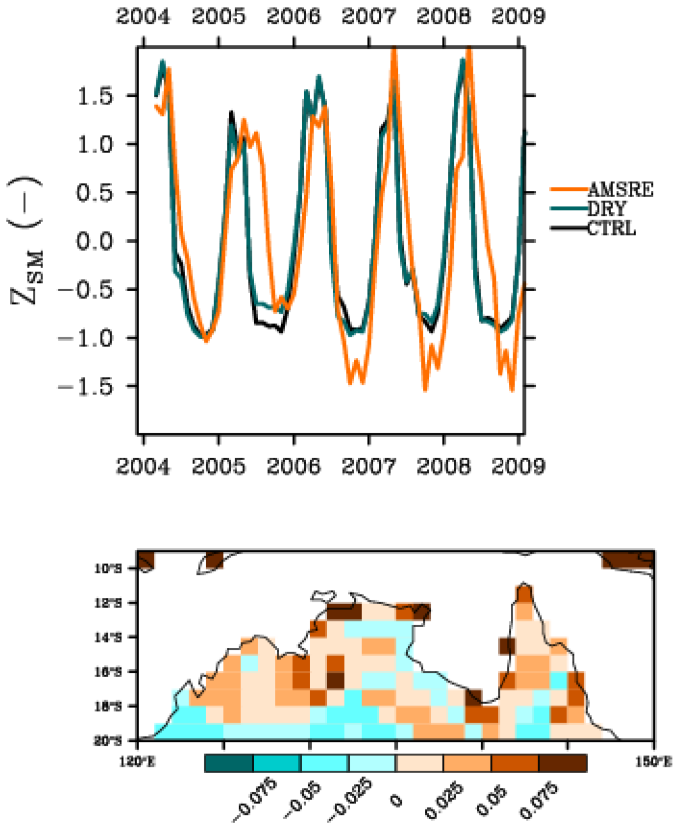

Figure 2. (a) The mean normalized (using the first two moments) first layer soil moisture (SM_1) from the CTRL and DRY simulations and the AMSR-E observations. (b) The difference between the mean SM_1 (from all simulations over all months from 2004-2009) and the AMSR-E observations.

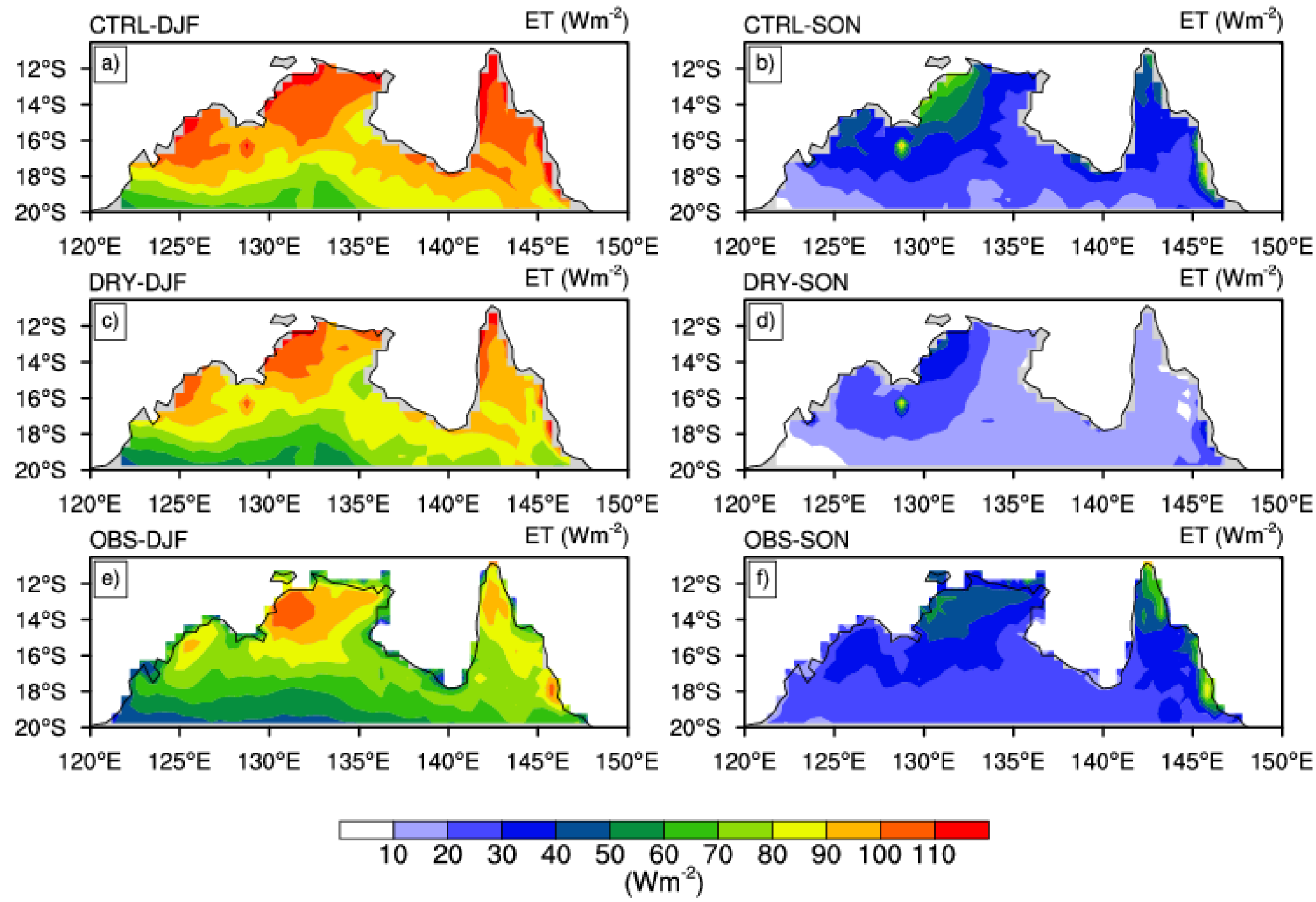

Figure 3. The mean ET (Wm^{-2}) from the wet season (DJF shown in the left hand column) and the transition between the dry and wet seasons (SON shown in the right hand column). The ensemble mean ET from (a) CTRL over DJF, (b) CTRL over SON, (c) DRY for DJF, (d) DRY from SON, (e) OBS (the mean of three gridded ET products) over DJF, and (f) OBS for SON.

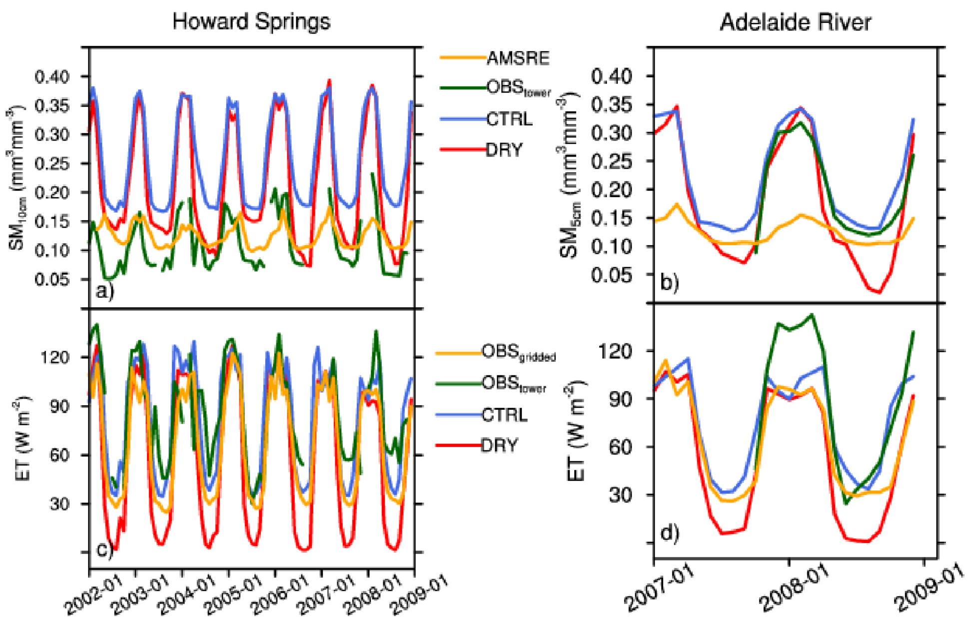

Figure 4. The monthly soil moisture (SM in mm^3mm^{-3}) from the ensemble mean from CTRL and DRY, AMSR-E, and flux tower measurements (OBS_{tower}) from flux tower sites at (a) Howard Springs at 10cm depth and (b) Adelaide River at 5cm depth. The monthly evapotranspiration (ET Wm^{-2}) from CTRL, DRY, the mean of three ET products ($OBS_{gridded}$) and the measurements at the (c) Howard Springs and (d) Adelaide River flux tower sites.

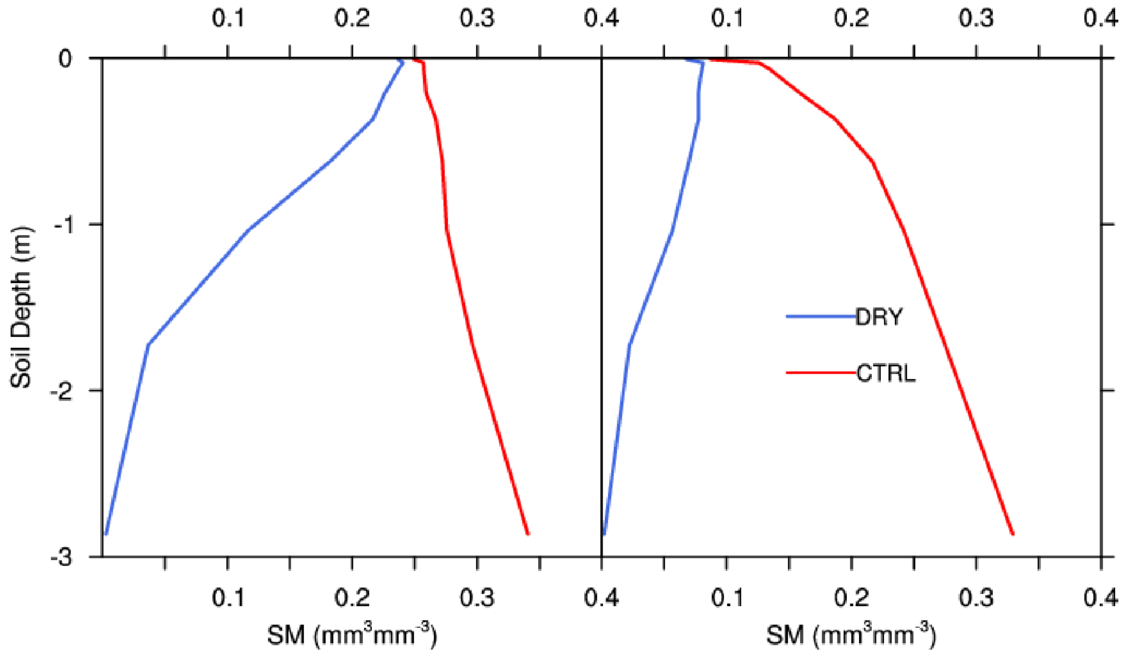

Figure 5. Spatiotemporal mean soil moisture (mm3mm-3) SM as a function of depth (m) for (a) DJF and (b) SON.

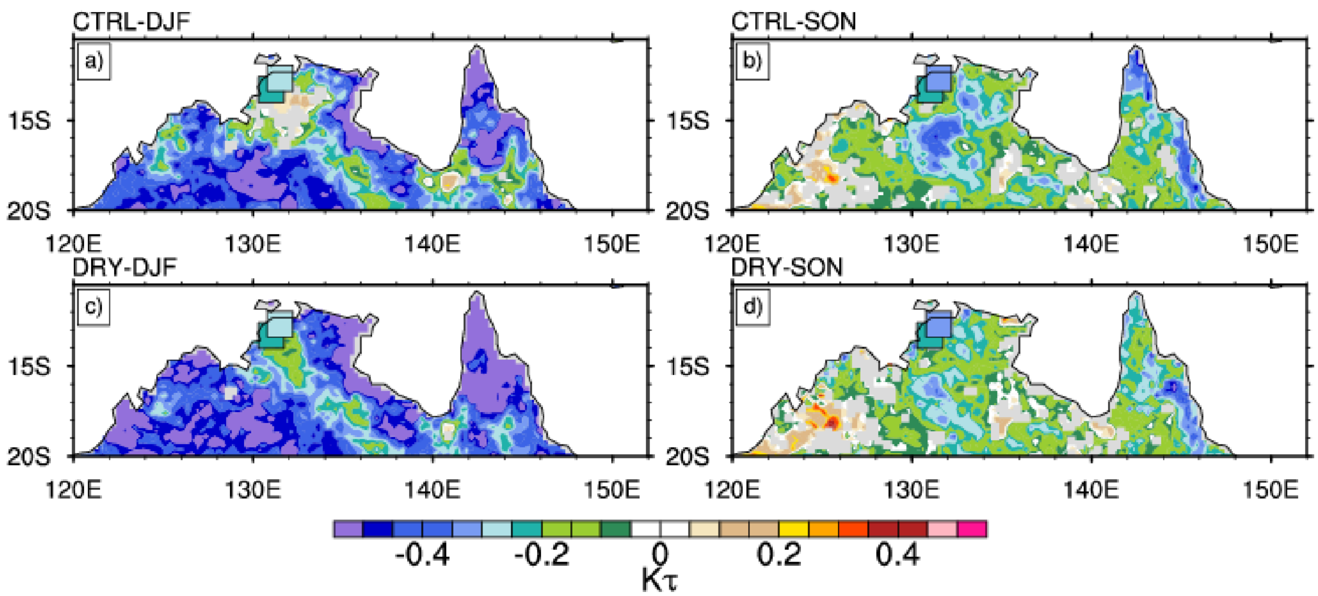

Figure 6. The ensemble median Kendall-tau correlation metric (Kτ) between the afternoon time (local) evaporative fraction (EF) and the afternoon computed lifting condensation level (LCL) at from (a) CTRL over DJF, (b) CTRL from SON, (c) DRY over DJF, and (d) DRY from SON. The black-outlined squares in (a)-(d) denote the values from the flux tower sites. Only statistically significant (95% confidence level) results are shown in (a)-(d).

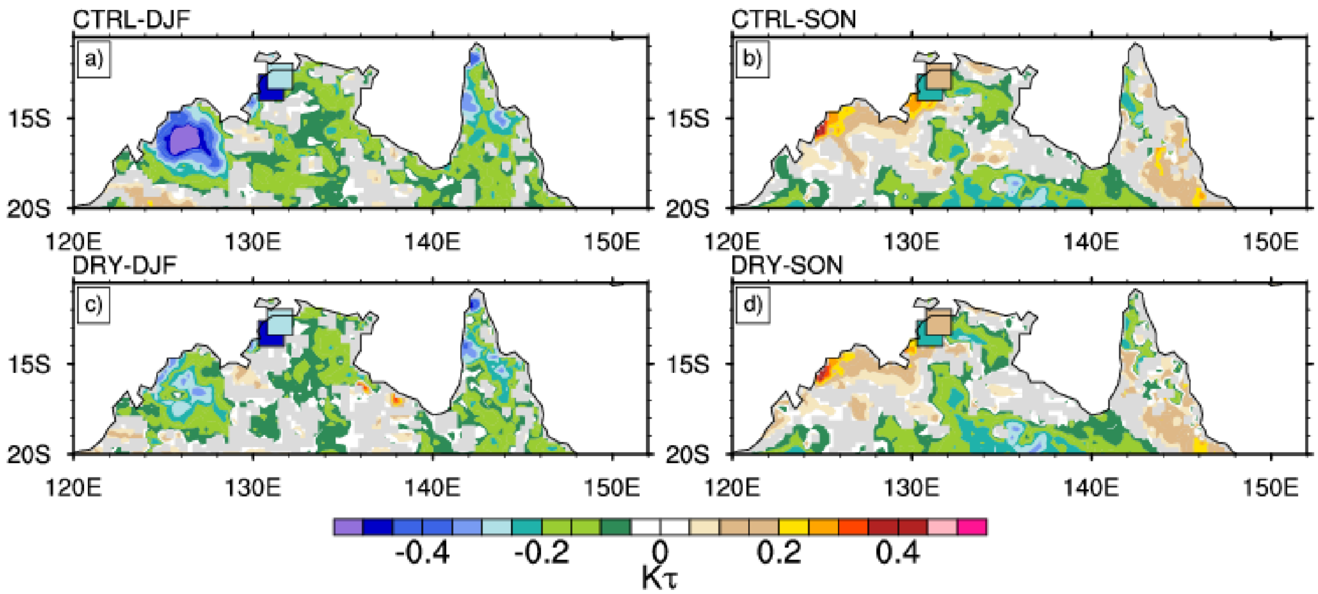

Figure 7. The ensemble median Kendall-tau correlation metric (Kτ) between the morning first layer soil moisture (SM_1) and the afternoon computed lifting condensation level (LCL) from (a) CTRL over DJF, (b) CTRL from SON, (c) DRY over DJF, and (d) DRY from SON. The black-outlined squares in (a)-(d) denote the values from the flux tower sites. Only statistically significant (95% confidence level) results are shown in (a)-(d).

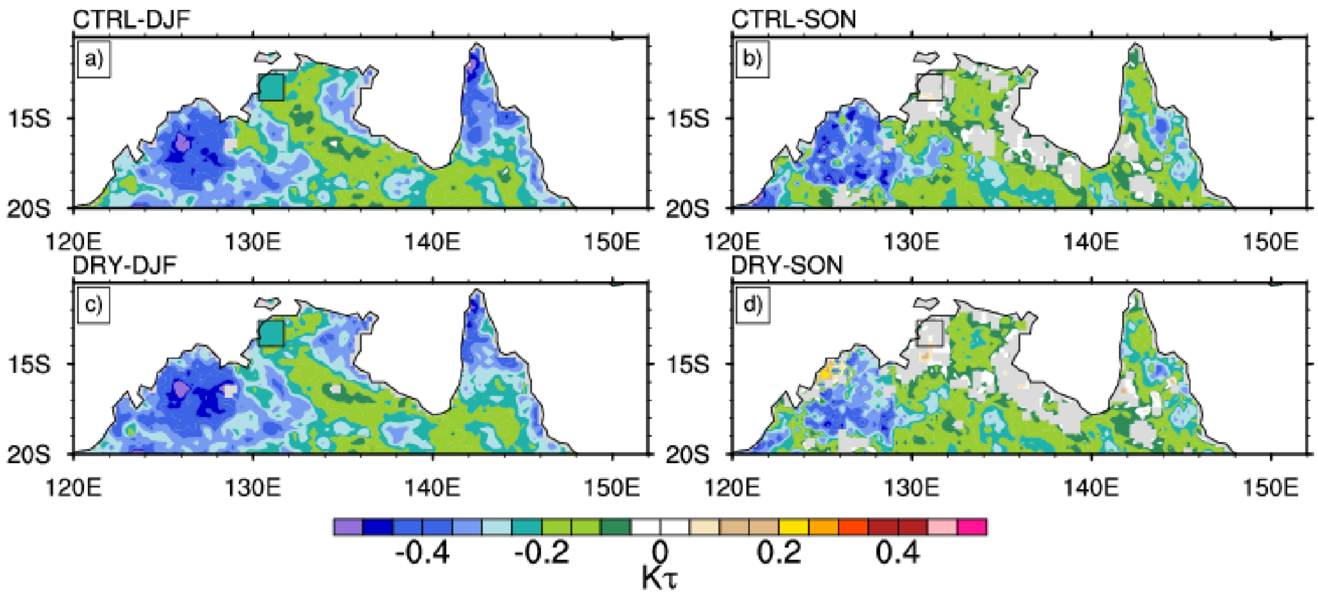

Figure 8. The ensemble median Kendall-tau correlation metric ($K\tau$) between the morning root zone soil moisture (SM_{rz}) and the afternoon computed lifting condensation level (LCL) from (a) CTRL over DJF, (b) CTRL from SON, (c) DRY over DJF, and (d) DRY from SON. The black-outlined squares in (a)-(d) denote the values from the Howard Springs flux tower site. Only statistically significant (95% confidence level) results are shown in (a)-(d).

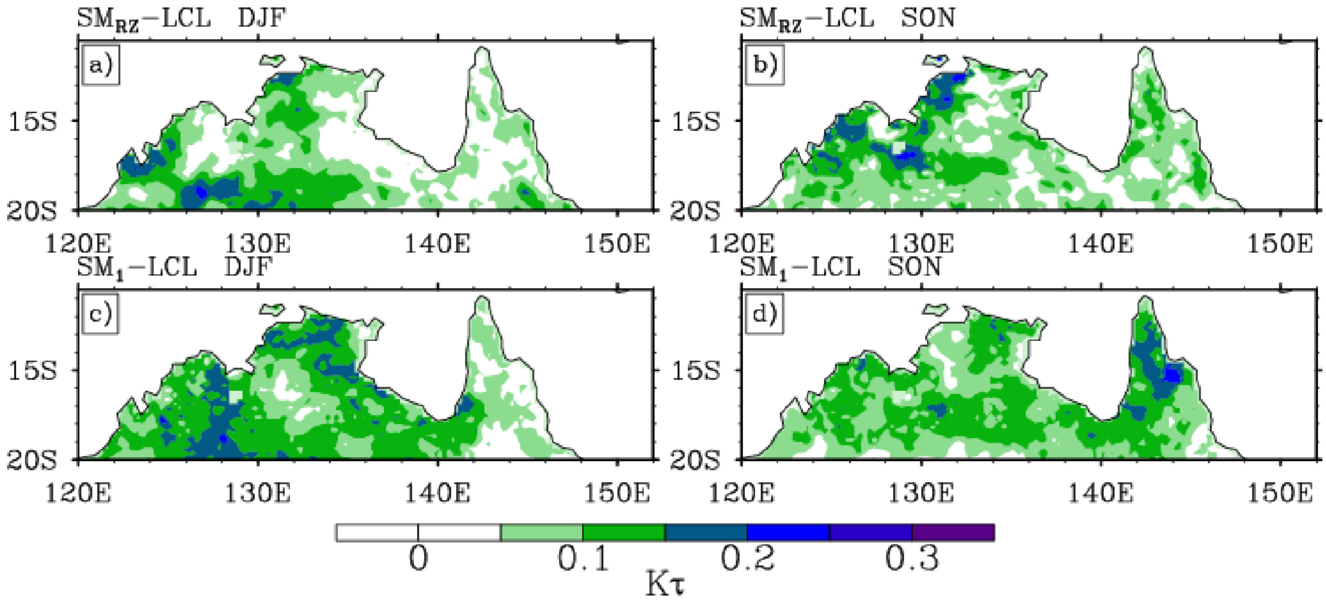

Figure 9. The standard deviation of the Kendall-tau correlation metric (Kτ) among the ensemble members between the afternoon computed lifting condensation level (LCL) and either the morning root zone soil moisture (SM_{rz}) over (a) DJF, (b) SON, or the morning first layer soil moisture (SM_1) over (c) DJF, and (d) SON.